Ionics
https://doi.org/10.1007/s11581-024-05747-3

RESEARCH

pH modulation for high capacity and long cycle life of aqueous zinc-ion batteries with β-MnO_2/3D graphene-carbon nanotube hybrids as cathode

Duolong Jin[1,2] · Xiaoping Dong[1,2] · Jiankai Liu[1,2] · Qianran Pang[1,2] · Shenghai Xin[1,2] · Liying Yang[1,2] · Cuibiao Wang[1,2]

Received: 26 May 2024 / Revised: 17 July 2024 / Accepted: 26 July 2024

Abstract

With the continuous development of new energy application technology, there is an increasingly urgent need for the safety and affordability of new energy storage products. In recent years, aqueous zinc-ion batteries based on mild aqueous electrolytes have garnered widespread attention as a potential replacement for traditional lithium-ion batteries. However, the limited capacity and low operating voltage of aqueous zinc-ion batteries restrict their widespread application. For this reason, sulfuric acid was added to the electrolyte, which effectively promotes the two-electron conversion of MnO_2/Mn^{2+} during the discharge process. This enhancement results in the high voltage segment of the batteries' discharge phase offering a higher reversible specific capacity. The results showed that the batteries with 0.1 M H_2SO_4 added to the electrolyte had a reversible discharge-specific capacity of up to 536.07 mAh·g^{-1} at a current density of 100 mA·g^{-1}. The activated batteries exhibited a reversible specific capacity of 85.11 mAh·g^{-1} even at a high current density of 1 A·g^{-1}. Furthermore, the capacity retention rate after 1000 cycles was 88.3%. Moreover, the activation rate of the batteries was faster with the addition of H_2SO_4, and the average operating potential increased compared to the batteries without H_2SO_4 in the electrolyte. This provides an effective solution for the practical application of aqueous zinc-ion batteries in power grids.

Keywords Aqueous zinc-ion battery · pH regulation of electrolyte · Electrochemical performance

Introduction

The extensive use of fossil fuels has led to increasingly serious environmental pollution problems. The pursuit of a green, safe, economically sustainable, and clean energy source has become a shared goal among all countries worldwide [1, 2]. In recent years, lithium-ion batteries have been widely used and promoted as a power source for new energy transportation and electronic equipment. However, significant environmental pollution problems and safety hazards exist in both their production and actual application [3, 4]. Aqueous zinc-ion batteries (AZIBs) based on a mild aqueous solution as an electrolyte have been favored by researchers due to their environmental friendliness, low cost, resourcefulness, high theoretical specific capacity, and lower potentials [5–9]. There are three main types of cathode materials for AZIBs [10]: manganese-based oxides [11, 12], vanadium-based oxides [13–17], and Prussian blue analogs [18, 19]. Among them, manganese-based oxides are the most common cathode materials for AZIBs, and MnO_2 is recognized as the primary cathode material for AZIBs. In order to enhance battery performance, various methods such as doping and mixing have been utilized to improve the structure of cathode materials [20–23]. Notably, the electrolyte is also a key component of batteries, providing a conducive working environment to ensure high compatibility and reversible cycling of the battery components. However, factors hindering the detachment of Zn^{2+}, such as cathodic dissolution, uncontrollable by-products, uncertainty in the storage mechanism, and insufficient energy density, still need to be resolved. These factors considerably limit the reversible specific capacity and cycling life of AZIBs [24–27].

✉ Xiaoping Dong
dxp0316@163.com

✉ Liying Yang
yangliying0116@163.com

[1] College of Quality and Technical Supervision of Hebei University, Baoding 071002, Hebei Province, China

[2] Technology Innovation Center of New Energy Vehicle Power System Lightweighting in Hebei Province, Baoding 071002, Hebei Province, China

Published online: 03 August 2024

Enhancing the performance of AZIBs on the basis of manganese-based cathode materials based on electrolyte modulation strategies has been extensively studied by scholars [28–32]. The first is to compare the effect of electrolytes with different anion compositions on the performance of batteries. Hu's [33] study found that the anion $CF_3SO_3^-$ in $Zn(CF_3SO_3)_2$ is bulky, which reduces solvation, and that $CF_3SO_3^-$ has less interaction with water compared to the $ZnSO_4$ electrolyte, which enhances electrochemical performance. Using zinc gluconate as an electrolyte, Xu [34] found that it not only stabilizes the supply of Zn^{2+}, but also acts as an interfacial stabilizer to provide gluconate anions, creating an artificially stabilized anionic interface and forming dendrite-free deposits; secondly, the addition of metal cation additives can effectively alleviate the dissolution of cathode materials according to the dissolution balance mechanism. Deng's [35] study achieved high specific capacity (326 $mAh{\cdot}g^{-1}$ at 100 $mA{\cdot}g^{-1}$) and excellent long-term cycling performance (stable capacity after 700 cycles at 2000 $mA{\cdot}g^{-1}$) based on the prepared MnO_2@CC cathode with electrolyte modulation with 3 M $ZnSO_4$ + 0.1 M $MnSO_4$. Zhang [36] innovatively used Mn^{2+} and Li^+ bimetallic anode electrolyte modulation to achieve a battery capacity of more than 300 $mAh{\cdot}g^{-1}$ with 1 M $ZnSO_4$ + 1 M $LiSO_4$ + 0.1 M $MnSO_4$ as the electrolyte under the synergistic effect of Mn^{2+} and Li^+ and up to 2000 long-term stability cycles at a high current density of 2 $A{\cdot}g^{-1}$. In addition, organic electrolyte additives (monosodium glutamate, threonine, eco-friendly silk peptides, etc.) play an important role in regulating the internal structure of solvents and inhibiting zinc dendrites in batteries [37–42]. It can be seen that in order to obtain long-life and highly stable AZIBs, attention must be paid to the electrolyte improvement strategy, and manganese-based oxides or hybrid cathode materials formed by them and carbon substances have excellent electrochemical performance under suitable electrolytes.

However, the theoretical specific capacity of conventional one-electron reactions based on the Mn^{4+}/Mn^{3+} redox couple is usually about 308 $mAh{\cdot}g^{-1}$, whereas it can be increased to 616 $mAh{\cdot}g^{-1}$ by a two-electron conversion mechanism (Mn^{4+}/Mn^{2+}). In order to construct a direct two-electron conversion mechanism of Mn^{4+}/Mn^{2+} and enhance the theoretical discharge-specific capacity of AZIBs, some scholars have made their own efforts, and through their respective innovative experiments, they have successfully realized the direct conversion of MnO_2 to Mn^{2+} at high operating voltage, which improves the discharge-specific capacity and the cycling life of AZIBs. Therefore, it is theorized that increasing the work potential of AZIBs by experimental methods will enhance the Mn^{4+}/Mn^{2+} two-electron conversion reaction [43, 44]. Unlike them, some scholars constructed the Mn^{4+}/Mn^{2+} two-electron conversion mechanism not by realizing a high operating voltage but by improving the structural properties of the cathode material or by electrolyte modulation. Li's study developed a nanoflower-like MnO_2/C composite as the anode material with 2.0 M $ZnSO_4$ + 0.5 M $MnSO_4$ as the electrolyte, and the results showed that the zinc-ion batteries with MnO_2/C as the cathode material could carry out a deep and fast reaction through the Mn^{4+}/Mn^{2+} two-electronic pathway, which was largely attributed to the advantages of the anode material such as fewer agglomerations, a larger specific surface area, and the presence of water of crystallization [45]. Zeng used an electrolyte modulation strategy and chose a mixed electrolyte salt of $Zn(CH_3COO)_2$ and $Mn(CH_3COO)_2$ for the two-electron redox reaction of Mn^{4+}/Mn^{2+} [46]. Zhong's study used acetate ions for electrolyte modulation, and they added CH_3COONa to the electrolytes of $ZnSO_4$ and $MnSO_4$ to achieve the MnO_2/Mn^{2+} conversion, the reason for this is reflected in the role of acetate ions, which promote the deposition of Mn^{2+} [47].

In this paper, we fabricated a hybrid of β-MnO_2/3D graphene-carbon nanotube cross-link (abbreviation: β-MnO_2/3D GPE-CNT) cathode material using a simple mechanical ball-milling method. This material exhibited excellent performance. Additionally, we introduced $MnSO_4$ and H_2SO_4 additives to the $ZnSO_4$ electrolyte. This method promotes the formation of a Mn^{4+}/Mn^{2+} two-electron conversion mechanism while ensuring the structural stability of cathode materials. In addition, we investigated the effects of different concentrations of H_2SO_4 on the electrochemical performance of the batteries. The results showed that the stabilized operating potential and discharge performance of the batteries improved with the addition of H_2SO_4. Specifically, batteries with 0.1 M H_2SO_4 in the electrolyte exhibited a reversible discharge-specific capacity of up to 536.07 $mAh{\cdot}g^{-1}$ at a current density of 100 $mA{\cdot}g^{-1}$. Furthermore, the activated batteries demonstrated a reversible specific capacity of 85.11 $mAh{\cdot}g^{-1}$ even under a high current density of 1 $A{\cdot}g^{-1}$, with a capacity retention rate of 88.3% after 1000 cycles. This work aims to offer a solution for large-scale energy storage applications using high-performance rechargeable aqueous Zn/MnO_2 batteries.

Experimental materials and methods

The original specimens used for the experiment were as follows: manganese dioxide (MnO_2, Xilong Science, China); zinc sulfate ($ZnSO_4$), manganese sulfate ($MnSO_4$), and N-methyl-2-pyrrolidone (NMP) were purchased from Aladdin, Italy; polyvinylidene fluoride (PVDF, Arkema, France); 3D graphene-carbon nanotubes (for microstructure see [48]); conductive carbon black (Super P, DENKA, Japan); parts of CR2032 button batteries.

The detailed preparation process of β-MnO_2/3D GEP-CNT hybrid cathode materials obtained by ball milling is described in [48, 49]. The mass ratio of β-MnO_2 to 3D GPE-CNT was 9:1, and the actual ball milling time was 2.5 h. The ball-milled cathode material, Super P, and PVDF were mixed homogeneously according to the mass ratio of 7:2:1 and then dripped into the appropriate amount of NMP solution, which was fully ground in an onyx mortar to obtain the slurry of cathode wafers. The slurry was uniformly coated on the surface of 316 stainless steel foil, and then placed in a vacuum drying oven at 110 °C for 12 h. A cutting machine was used to cut the dried specimen sheet into a circular sheet with a diameter of about 14 mm as the positive electrode sheet, and the average mass density of the active substance on the positive electrode sheet was about 0.49 $mg{\cdot}cm^{-2}$. Then, it is assembled with zinc sheet negative electrode, electrolyte, and glass fiber diaphragm to form CR2032 type button batteries, where the electrolyte is (2M $ZnSO_4$ + 0.5M $MnSO_4$ + 0.05, 0.1, 0.2, 0.3 M H_2SO_4) solution respectively.

X-ray diffraction analysis (XRD, SmartLab), field emission scanning electron microscope (FSEM, Hitachi S-4800), transmission electron microscope (TEM, JEOL JEM 2800), laser particle size analyzer (Malvern 3000), and specific surface pore size analyzer (JW-BK200B) were used to test the phase structure, particle morphology, atomic arrangement, particle size distribution, and specific surface area size of the β-MnO_2/3D GEP-CNT hybrid anode material, respectively. The assembled batteries were allowed to stand for more than 6 h. Constant-current charge/discharge tests were performed in a Neware battery tester (Model CT-4008) at different current densities in the range of 100 $mA{\cdot}g^{-1}$ to $1A{\cdot}g^{-1}$, and electrochemical impedance spectroscopy was carried out in an electrochemical workstation (Model CHI660) with frequency scans ranging from 0.01 Hz to 100 kHz. The cyclic voltammetry (CV) curves were tested at scanning rates of 0.1, 0.2, 0.3, 0.4, and 0.5 $mv{\cdot}s^{-1}$.

Results and discussion

The results of the microstructure tests are described in detail in and will not be repeated here [48, 49]. As shown in Fig. 1a–c, the results of SEM and TEM tests showed that the hybrids after ball milling were distributed as spherical particles, the phenomenon of agglomeration was obviously reduced, and the ball milling greatly reduced the particle size of the anode material, which led to the increase of the specific surface area of the material. As shown in Fig. 1d, the XRD patterns related to MnO_2 in the β-MnO_2/3D GEP-CNT hybrids matched the standard card (JCPDS: 39-0375) for β-MnO_2, and the phase structure of the samples was not significantly altered before and after ball milling. The results of the particle size test are given in Fig. 1e, and the average particle size of the sample obtained by the laser particle size analyzer was 20.33 μm. XPS tests of the ball-milled styles are given in Fig. 1f, and the results show that the peak positions and the peak value of Mn2p did not change significantly after ball milling.

Inspired by the above, the deepening of the MnO_2/Mn^{2+} conversion reaction can also be effectively promoted under the suitable cathode material or electrolyte, thus providing higher reversible specific capacity and stable charging/discharging cycles for AZIBs. In our previous studies, we have demonstrated that β-MnO_2/3D GEP-CNT cathode materials have properties such as low agglomeration and high specific surface area, which are favorable for Zn^{2+} insertion and extraction, and the reversible specific capacity of the batteries is improved compared with that of ordinary β-MnO_2 cathode materials [48]. With 2.0 M $ZnSO_4$ + 0.5 M $MnSO_4$ as the electrolyte, the specific capacity of the batteries reached 521.91 $mAh{\cdot}g^{-1}$ after activation, and we proved the existence of an indirect conversion mechanism of MnO_2/Mn^{2+} by electrochemical tests [49]. In order to further deepen this two-electron conversion mechanism, we continued to add different concentrations of H_2SO_4 to the above electrolyte. The capacity decay curves of the batteries at a current density of 100 $mA{\cdot}g^{-1}$ with different concentrations of H_2SO_4 solutions pre-added to the electrolyte are shown in Fig. 2a. The discharge-specific capacity of the β-MnO_2/3D GEP-CNT cathode material reached 302.37 $mAh{\cdot}g^{-1}$ after activation when 2.0 M $ZnSO_4$ + 0.5 M $MnSO_4$ + 0.05 M H_2SO_4 solution was used as the electrolyte, which was higher than that when $ZnSO_4$ solution was used as the electrolyte alone, and the capacity decay was very slow when the batteries were stabilized. The combination of previous studies suggests that it is the $MnSO_4$ in the electrolyte that plays a role, and that it inhibits the capacity degradation of the batteries well. However, the addition of 0.05 M H_2SO_4 did not further enhance the performance of the batteries, such as the activation rate and reversible specific capacity, as expected from the original electrolyte (2.0 M $ZnSO_4$ + 0.5 M $MnSO_4$). It is hypothesized that this may be due to the fact that although the addition of H_2SO_4 to the electrolyte is conducive to the promotion of H^+ insertion, it may not be conducive to the insertion reaction of Zn^{2+} so the batteries rely on the transfer of Zn^{2+} to release less capacity, thus limiting the capacity of the batteries, which is verified by the electrochemical tests that follow. We continued to increase the concentration of H_2SO_4 in the electrolyte in the hope that the batteries would provide a large amount of discharge-specific capacity during the high voltage phase of the discharge process, which could offset the decrease in the total discharge-specific capacity caused by the lower discharge capacity in the low voltage phase. As we envisioned, the discharge-specific capacity of the batteries was greatly improved when the concentration of H_2SO_4 in the electrolyte

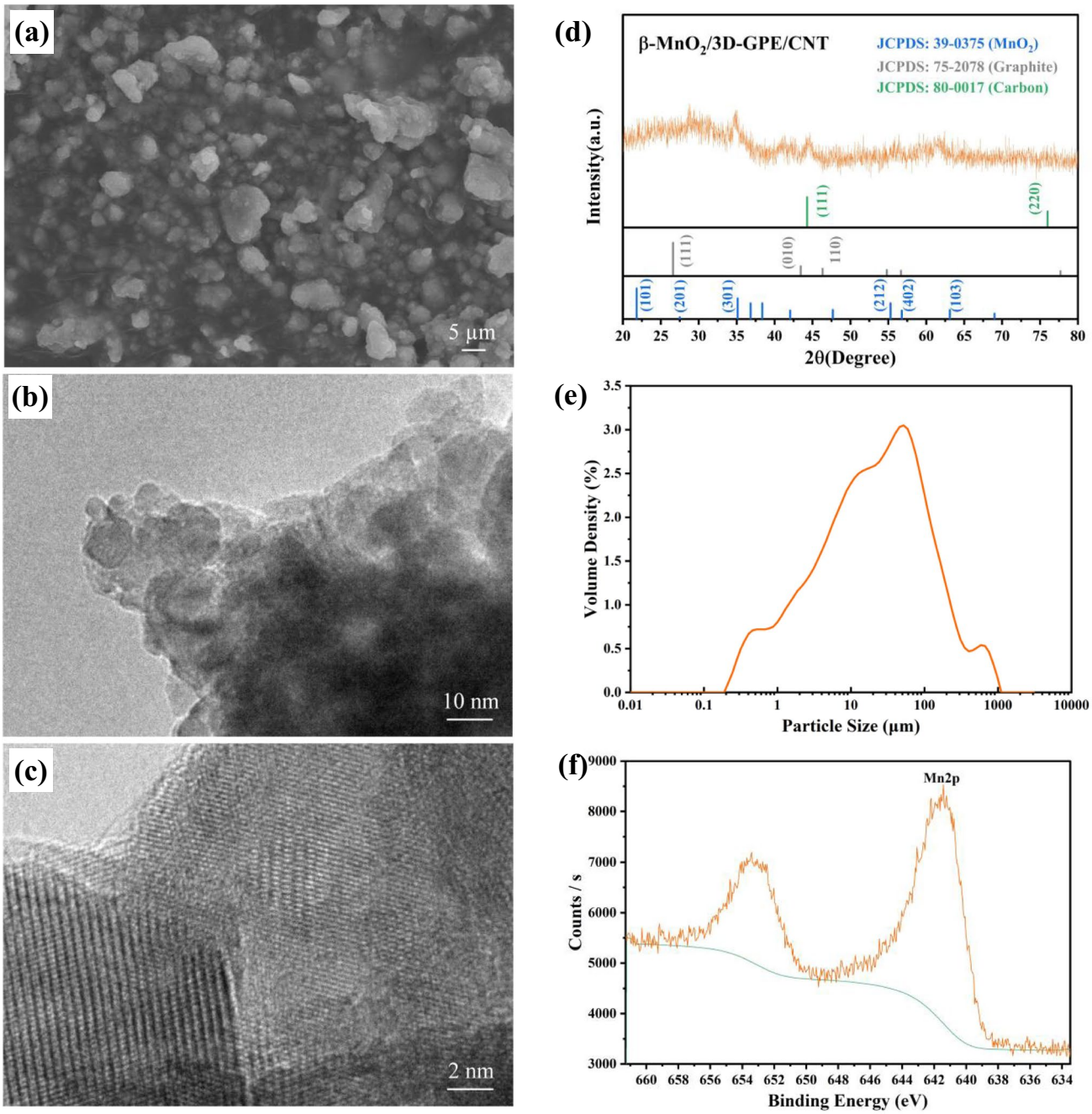

Fig. 1 Microcosmic characterization Chart. **a** SEM image of β-MnO_2/3D GEP-CNT; **b** and **c** TEM image of β-MnO_2/3D GEP-CNT; **d** XRD image of β-MnO_2/3D GEP-CNT; **e** particle size test image of β-MnO_2/3D GEP-CNT; **f** XPS image of β-MnO_2/3D GEP-CNT

reached 0.1 M with good capacity retention. As shown in Fig. 2a, the discharge-specific capacity of the batteries with 2.0 M $ZnSO_4$ + 0.5 M $MnSO_4$ + 0.1 M H_2SO_4 solution as the electrolyte rapidly climbed up after a period of activation, with a more desirable activation rate. After full activation, the discharge-specific capacity of the batteries reached 536.07 mAh·g^{-1}, and the capacity was well maintained, and the discharge-specific capacity remained at 446.57 mAh·g^{-1} after 100 cycles. This indicates that under appropriate acidic conditions, batteries can also provide considerable discharge-specific capacity through the chemical reaction in the high voltage phase, and this phase of the discharge reaction is often accompanied by the Mn^{4+}/Mn^{2+} two-electron conversion, which has a higher theoretical specific capacity, and if we utilize this phase well, and provide a larger portion of the discharge-capacity of the battery from this phase, then

we can further enhance the discharge-specific capacity of AZIBs. This phenomenon is similar to the studies by Zeng [46] and Zhong [47] and Chao [50], among others. A small portion of the capacity of the batteries decayed during the later cycles, due to the pH shift of the battery during the reaction, and as the reaction proceeds, the overall pH of the electrolyte rises so that the sulfuric acid's effect in the electrolyte diminishes. The study by Christian [51] and his colleagues revealed the above pH change process well by adding a pH-indicating instrument to the electrolyte, which was later verified by electrochemical tests. However, when we continued to increase the concentration of the H_2SO_4 solution, the electrochemical performance of the batteries did not improve further, and the discharge-specific capacity of the batteries with 2.0 M $ZnSO_4$ + 0.5 M $MnSO_4$ + 0.2 M H_2SO_4 solution as the electrolyte batteries did not improve substantially in the pre-reaction period, and the specific capacity also decreased and could only reach 427.72 $mAh{\cdot}g^{-1}$. With the addition of 0.3 M H_2SO_4 solution, the electrochemical performance of the batteries was even worse, and the discharge-specific capacity could only reach 358.91 $mAh{\cdot}g^{-1}$, and the activation rate was even slower, with poor capacity retention and stability. This is due to the enhanced hydrogen precipitation reaction in AZIBs under more acidic conditions, which can deplete the H^+ in the electrolyte and cause the pH of the electrolyte to increase, thereby affecting the electrochemical performance of the batteries. Figure 2b exhibits the GCD curves for the addition of different concentrations of H_2SO_4 to the electrolyte at a greater current density of 500 $mA{\cdot}g^{-1}$. It can be seen that the discharge-specific capacities of the batteries can reach 164.84 $mAh{\cdot}g^{-1}$, 225.26 $mAh{\cdot}g^{-1}$, 199.61 $mAh{\cdot}g^{-1}$, and 182.96 $mAh{\cdot}g^{-1}$ with the addition of 0.05, 0.1, 0.2, and 0.3 M H_2SO4 solution, respectively, and the capacity change trends as well as the activation rate and other properties are similar to those at 100 $mA{\cdot}g^{-1}$ current density. To further test the cycling performance of these batteries after the addition of H_2SO4 solution to the electrolyte, we performed the GCD test at a high current density of 1 $A{\cdot}g^{-1}$, and the results are shown in Fig. 2c. It can be seen that the batteries have excellent cycle life and electrochemical stability when adding 0.1 M H_2SO_4 solution to the electrolyte, and the discharge-specific capacity of the batteries can reach 121.57 $mAh{\cdot}g^{-1}$ and the capacity retention rate is 88.3% after 1000 cycles. To further investigate the effect of different concentrations of H_2SO_4 solution added to the electrolyte on the discharge process of the batteries, the capacity versus voltage curves of the batteries during the charging and discharging process are given in Fig. 2d. As can be seen from the figure, the discharge capacity of the batteries in the high voltage phase (1.8~1.5 V) was enhanced after the addition of H_2SO_4, and the difference in the capacity contribution of this phase under different concentrations of H_2SO_4 was not significant, which also verified the conclusion of the deepening of the discharge reaction in the high voltage phase under the acidic condition as stated earlier. Moving on to this figure, the substantial increase in capacity at 0.1 M H_2SO_4 compared to 0.05 M H_2SO_4 is mainly attributed to the capacity contribution of the chemical reaction at voltages lower than 1.5 V. This also proves that 0.1 M H_2SO_4 is a suitable concentration because it not only promotes the two-electron conversion reaction in the high voltage phase, but also does not interfere with the embedded detachment of Zn^{2+}, thus increasing the batteries' discharge-specific capacity, which also verifies the previous hypothesis. The effect of hydrogen precipitation reaction at high H_2SO_4 concentration can also be seen from this figure; the capacity contribution of the low voltage phase is gradually weakened as the H_2SO_4 concentration continues to increase from 0.1 M to 0.2 M or even 0.3 M, which is the reason for the capacity decrease at high H_2SO_4 concentration. In Fig. 2e, we roughly divide the discharge process of the batteries under 0.1 M H_2SO_4 into three stages, D1 (1.8~1.5 V), D2 (1.5~1.25 V), and D1 (1.25~1.0 V), and analyze the capacity versus voltage curves of the batteries under the addition of 0.1 M H_2SO_4 during the cycling process. It can be seen that the discharge capacity at each stage of the cycling process has different degrees of growth, and in the first lap of the cycle, the proportion of the capacity higher than 1.2 V to the total capacity is above 90%, and this proportion gradually decreases as the cycle proceeds, which once again confirms the conclusion that the pH of the electrolyte rises in the course of the reaction. In order to compare the changes in the charging and discharging process of the batteries before and after the addition of 0.1 M H_2SO_4 more intuitively, the comparative graphs of the GCD curves before and after the addition of 0.1 M H_2SO_4 as well as the curve of the change in the discharging capacity versus the voltage are given in Fig. 2f and g, respectively. It can be seen that the activation rate of the batteries is faster after adding 0.1 M H_2SO_4, and there is a substantial increase in specific capacity after 10 cycles, compared to the batteries without H_2SO_4 where the capacity rises substantially only after 20 cycles. In addition to this, the capacity of the batteries with 0.1 M H_2SO_4 added at the end of activation decays to a lesser extent, which is consistent with the previous analysis.

CV curves were utilized to further investigate the electrochemical performance of batteries with β-MnO_2/3D GEP-CNT as the cathode material at different concentrations of H_2SO_4 as the electrolyte additive. The CV test results are shown in Fig. 3, where the position of each redox peak of the CV curve, the magnitude of the peak current, and the area of the CV curve correspond to the previous charge/discharge test process. The CV curves of the batteries with 2.0 M $ZnSO_4$ + 0.5 M $MnSO_4$ + 0.05 M H_2SO_4 solution as the electrolyte are given in Fig. 3a, and it can be seen that

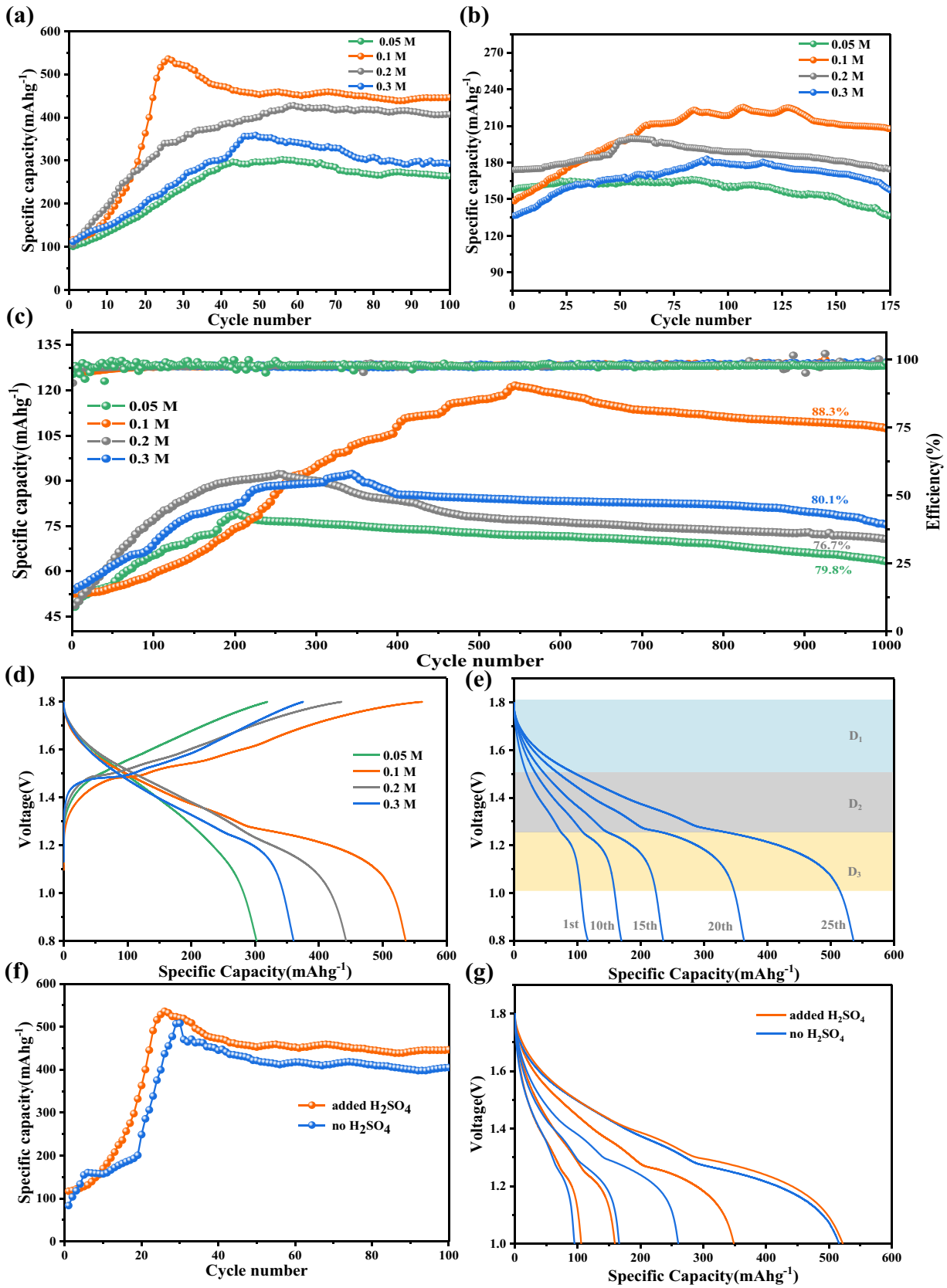
(a)
Specific capacity(mAhg-1)
Cycle number
0.05 M
0.1 M
0.2 M
0.3 M
(b)
Specific capacity(mAhg-1)
Cycle number
0.05 M
0.1 M
0.2 M
0.3 M
(c)
Specific capacity(mAhg-1)
Efficiency(%)
Cycle number
0.05 M
0.1 M
0.2 M
0.3 M
88.3%
80.1%
76.7%
79.8%
(d)
Voltage(V)
Specific Capacity(mAhg-1)
0.05 M
0.1 M
0.2 M
0.3 M
(e)
Voltage(V)
Specific Capacity(mAhg-1)
D1
D2
D3
1st
10th
15th
20th
25th
(f)
Specific capacity(mAhg-1)
Cycle number
added H2SO4
no H2SO4
(g)
Voltage(V)
Specific Capacity(mAhg-1)
added H2SO4
no H2SO4

◂**Fig. 2** GCD test result image. **a** GCD curves at 100 mA·g^{-1} with the addition of different concentrations of H_2SO_4; **b** GCD curves at 500 mA·g^{-1} with the addition of different concentrations of H_2SO_4; **c** GCD and Coulomb efficiency curves at 1 A·g^{-1} with the addition of different concentrations of H_2SO_4; **d** charge-discharge capacity-voltage curves at 100 mA·g^{-1} with different concentrations of H_2SO_4 added to the electrolyte; **e** charge-discharge voltage curves of the electrolyte as 2M $ZnSO_4$ + 0.5M $MnSO_4$ + 0.1M H_2SO_4 during cycling; **f** comparison curves of GCD at 100 mA·g^{-1} before and after addition of 0.1 M H_2SO_4; **g** discharge capacity-voltage curve before and after adding 0.1M H_2SO_4

the CV curves show three reduction peaks (Peak5, Peak3, and Peak4) near 1.25 V, 1.35 V, and 1.45 V. The first two reduction peaks are consistent with those in the previous study (with 0.5M MnSO4 additive only, shown in Fig. 3i), which corresponded to the conversion reaction that produced by-products and the insertion reaction of Zn^{2+}, respectively [49]. The oxidation peaks Peak1 and Peak2 correspond to the Zn^{2+} and H^+ removal reactions, respectively. It is observed that, with the increase of scanning rate, the peak currents of each peak of its CV curve gradually increase, the positions of Peak1 and Peak2 move to the direction of high voltage, while Peak3, Peak4, and Peak5 move to the direction of low voltage, and the CV curves can keep similar shapes, indicating that the cathode material has good reversibility.

$$i = av^b \tag{1}$$

$$\lg(i) = blg(v) + \lg(a) \tag{2}$$

The type of electrochemical kinetics of the cathode material can be determined by Eqs. (1) and (2) above. where a and b are variable parameters, i denotes the peak current, and v is the scan rate. a and b correspond to the intercept and slope of the linearly fitted log(i)-log(v) plots, respectively, and when b is closer to 0.5, it indicates that the ion migration during the reaction is dominated by diffusive behavior, while when b is closer to 1, it indicates that the capacitive behavior is dominant [52]. As can be seen from Fig. 3b, the parameters b of Peak1~Peak5 are 0.73, 0.57, 0.67, 0.62, and 0.55, respectively, which are all closer to 0.5, indicating that the insertion/extraction reactions of H^+ and Zn^{2+} are diffusion-controlled.

We continued to study the CV curves at high H_2SO_4 concentrations. From Fig. 3c, e, and g, it can be clearly seen that the reduction peaks corresponding to Peak5 are not obvious or even disappeared when the concentration of H_2SO_4 is increased to 0.1 M, 0.2 M, and 0.3 M, indicating that the provision of the discharge capacity of the batteries is dominated by the reactions corresponding to Peak3 and Peak4, and this result is in line with the results of the previous GCD test, which once again illustrates that the addition of electrolyte H_2SO_4 can significantly increase the capacity contribution in the discharge phase of the high voltage phase, providing batteries with higher discharge-specific capacity [53]. It is clear from Fig. 3d, f, and h that the b is still close to 0.5 at this point, again demonstrating that the electrochemical behavior of the batteries is also dominated by diffusion, which behaved consistently with no addition of sulfuric acid (as shown in Fig. 3j). The reason for the deterioration in capacity when adding H_2SO_4 at concentrations higher than 0.1 M can also be clued from the CV curves. As can be seen from Fig. 3e and g, compared with the CV curves at 0.1 M, the shapes of the reduction peak Peak4 in the CV curves at 0.2 M and 0.3 M do not shift much, suggesting that the insertion reaction of H^+ can also be positively affected at high concentrations of H_2SO_4. The difference is that the peak current of the reduction peak Peak3 decreases and its shape becomes less pronounced, which suggests that the hydrogen precipitation reaction caused by the high concentration of H_2SO_4 in the electrolyte adversely affects the insertion of Zn^{2+}, which is more serious at 0.3 M H_2SO_4, which is again in full agreement with the previous GCD test results. It is again confirmed that acidic conditions at appropriate pH are more favorable for the formation of Zn^{2+} and H^+ co-embedded detachment mechanism to provide higher reversible specific capacity of the batteries, whereas hydrogen precipitation reaction is highly susceptible to occur under acidic conditions at lower pH, which impairs the discharge capacity and cycling stability of the batteries.

To further illustrate the embedding/de-embedding rate of Zn^{2+} in the batteries at different concentrations of H_2SO_4 as an electrolyte additive, the EIS-fitted Nyquist curves of the batteries at different concentrations of H_2SO_4 as electrolyte additive in the frequency range of 0.01 Hz~10 kHz as well as the Warburg impedance plots are presented in Fig. 4a and b, respectively. The rate of Zn^{2+} embedding/de-embedding in batteries can be reflected by the bulk-phase ion diffusion coefficient (D_{ion}) with the following equation:

$$D_{ion} = \frac{R^2T^2}{2n^4F^4A^2{C_{ion}}^2\sigma^2} \tag{3}$$

where R is the gas constant, T is the operating temperature of the batteries (thermostat set temperature value of 298.15 K), n is the number of electrons transferred in each molecule, F is Faraday's constant, A is the area of the electrode (1.54 cm^2), and C_{ion} is the concentration of the ions in the active substance. σ is the Warburg factor, corresponding to the slope of the Warburg impedance curve (Z'-$\omega^{-1/2}$) in Fig. 4b slope, and a smaller σ indicates a larger diffusion coefficient D_{ion}. Compared with the previous study, it can be seen that the σ value when using 2.0 M $ZnSO_4$ + 0.5 M $MnSO_4$ + 0.1 M H_2SO_4 as electrolyte is only 3.59, which is smaller

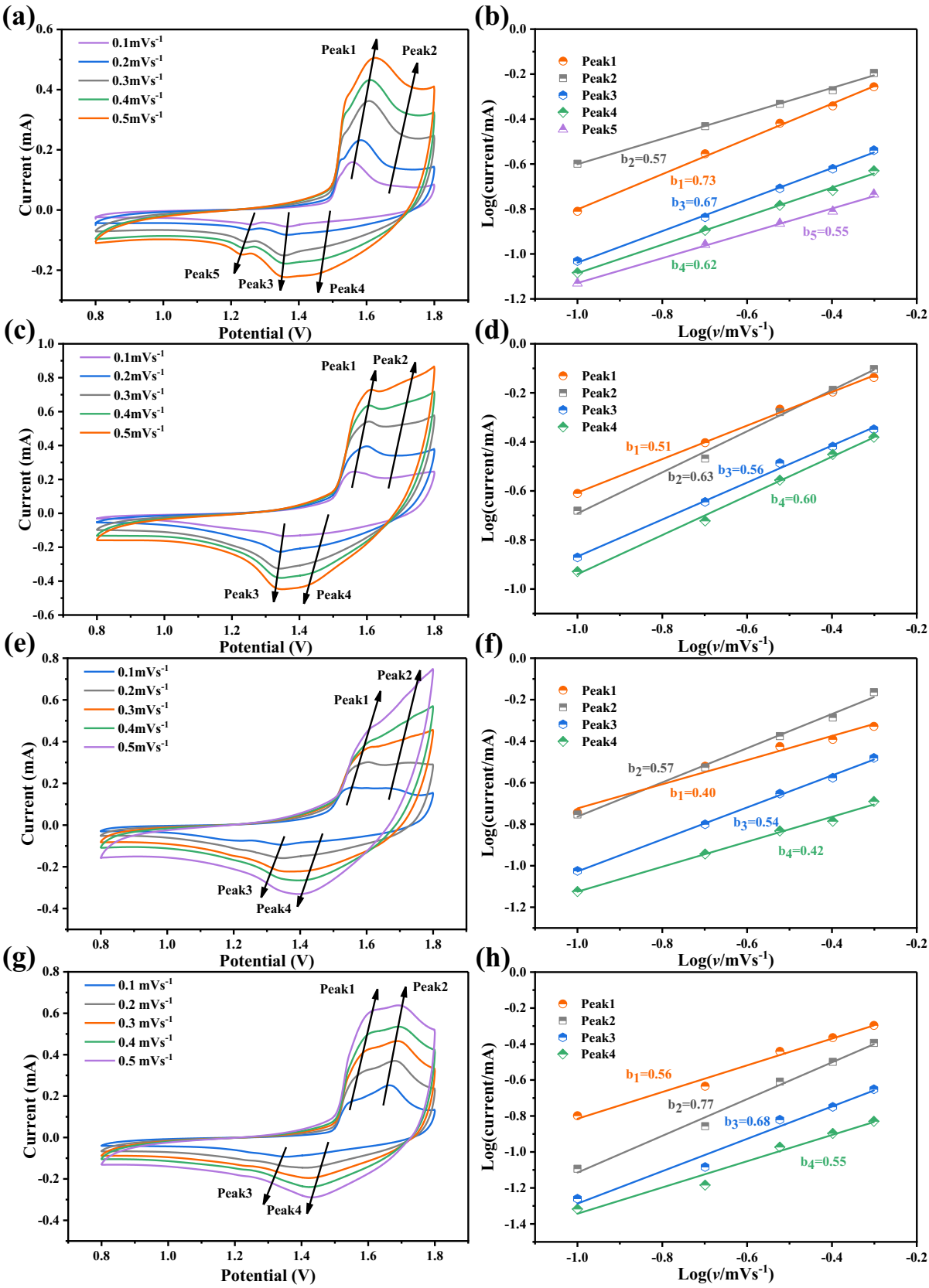

Fig. 3 CV test curve and their linearly fitted log(*i*)-log(*ν*) plots. **a** and **b** are the CV and log(*i*)-log(*ν*) plot with the addition of 0.05 M H_2SO_4; **c** and **d** are the CV and log(*i*)-log(*ν*) plot with the addition of 0.1 M H_2SO_4; **e** and **f** are the CV and log(*i*)-log(*ν*) plot with the addition of 0.2 M H_2SO_4; **g** and **h** are CV and log(*i*)-log(*ν*) plot for the addition of 0.3 M H_2SO_4; **i** and **j** are CV and log(*i*)-log(*ν*) plot for the addition of 0.5 M $MnSO_4$ without H_2SO_4

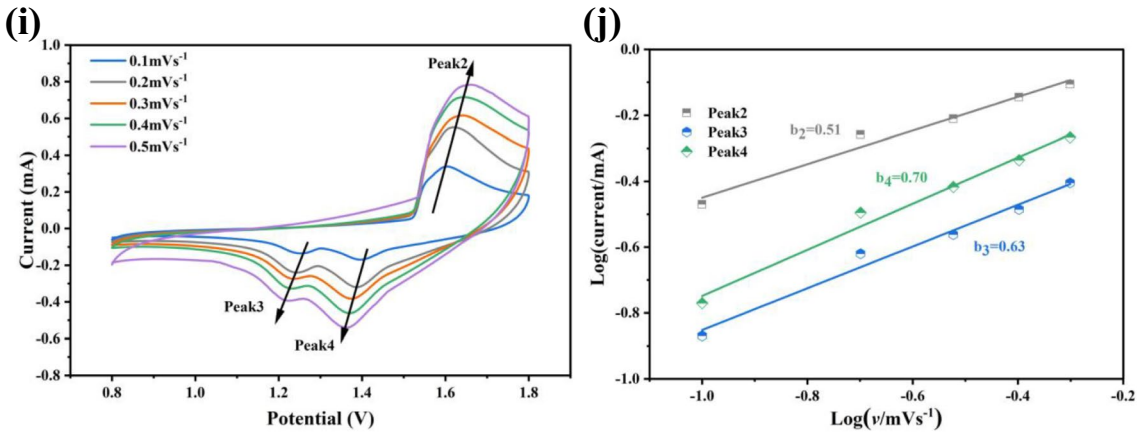

Fig. 3 (continued)

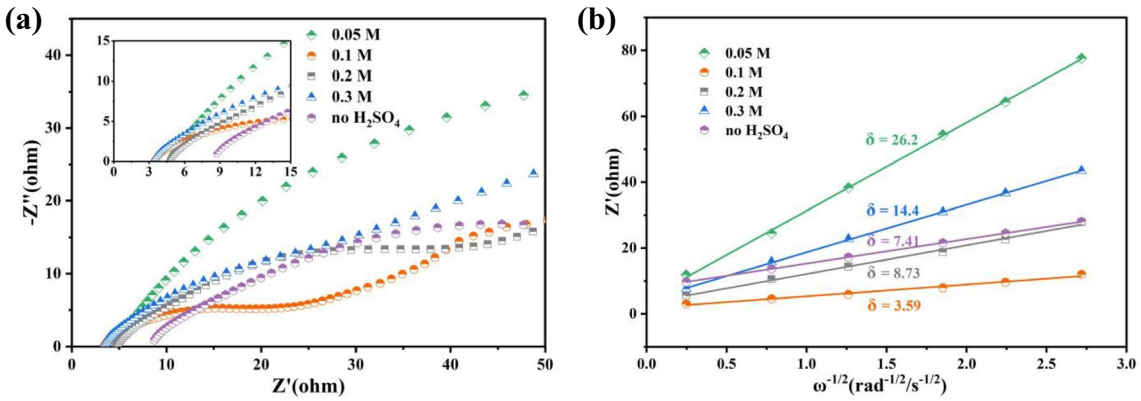

Fig. 4 EIS test and its fitted Warburg curve. **a** EIS curves with the addition of different concentrations of H_2SO_4; **b** fitted Warburg curves with different concentrations of H_2SO_4 added

than when using 2M $ZnSO_4$ + 0.5M $MnSO_4$ as electrolyte ($\sigma = 7.41$). The σ values when adding other lower or higher concentrations of H_2SO_4 as an electrolyte are all larger than when using 2 M $ZnSO_4$ + 0.5 M $MnSO_4$ as an electrolyte alone. The calculated $D_{ion}(Zn^{2+})$ with the addition of 0.1 M H_2SO_4 was 1.17×10^{-11} $cm^2 \cdot s^{-1}$ higher than that with 2M $ZnSO_4$ + 0.5M $MnSO_4$ as electrolyte, which was 2.74×10^{-12} $cm^2 \cdot s^{-1}$ [49].

Combined with the above electrochemical performance analysis and related studies, it was demonstrated that the β-MnO_2/3D GPE-CNT AZIBs complied with the H^+ and Zn^{2+} co-insertion/extraction mechanism and successfully realized the Mn^{4+}/Mn^{2+} two-electron conversion mechanism after the addition of H_2SO_4, with the following reaction principle:

Cathode:

$$MnO_2 + 4H^+ + 2e^- \leftrightarrow Mn^{2+} + 2H_2O \quad (4)$$

$$MnO_2 + H^+ + e^- \leftrightarrow MnOOH \quad (5)$$

$$yMnO_2 + xZn^{2+} + 2xe^- \leftrightarrow Zn_x(MnO_2)_y \quad (6)$$

Anode:

$$Zn - 2e^- \leftrightarrow Zn^{2+} \quad (7)$$

where Eqs. (4) and (5) correspond to Mn^{4+}/Mn^{2+} two-electron transitions as well as Mn^{4+}/Mn^{3+} one-electron transitions, respectively. The two-electron conversion reaction of Eq. (4) takes place at the higher voltage discharge stage D1, and the one-electron conversion reaction of Eq. (5) takes place at the lower voltage D2. The electrochemical test results show that we can actually view the D1 and D2 discharge phases as a whole, and although the two-electron conversion reaction of MnO_2/Mn^{2+} takes place in the higher voltage discharge phase, there is no clear voltage

boundary between the one-electron and two-electron reactions, and the two-electron conversion is much deeper and contributes to a higher percentage of the total capacity of the discharge under the appropriate pH conditions. This view is similar to the study by Zhong [47] and his colleagues. Equation (6) corresponds to the insertion reaction of Zn^{2+}, for which the reaction principle is also described in detail [54]. The successful construction of the Mn^{4+}/Mn^{2+} two-electron conversion mechanism is actually also inextricably linked to the excellent performance of our prepared anode materials, as summarized in the following overview: (1) The lamellar structure of β-MnO_2 is suitable for the insertion and detachment of H^+ and Zn^{2+}; (2) Ball milling greatly reduces the particle size of β-MnO_2, which leads to a reduction in the agglomeration phenomenon, and the β-MnO_2 particles are more dispersed, and the ion diffusion is accelerated; (3) The specific surface area of the cathode material increased after ball milling, and the active sites attached to the β-MnO_2/3D GEP-CNT hybrid material were more easily contacted with the electrolyte; (4) The excellent performance of 3D graphene-carbon nanotubes enhanced the conductivity of the cathode material.

Considering that zinc reacts easily with sulfuric acid, we then explored the stability of the zinc anode in the electrolyte. We found from our observation experiments that in this electrolyte with a low concentration of sulfuric acid added, the consumption of zinc was not obvious, and there was no bulging of the reacted batteries, and the mass and morphology of the reacted zinc flakes did not change much compared with those without sulfuric acid added. Then, the surface characteristics of the zinc anode before and after the reaction were carefully observed with an optical microscope. Figure 5a–c are the actual pictures

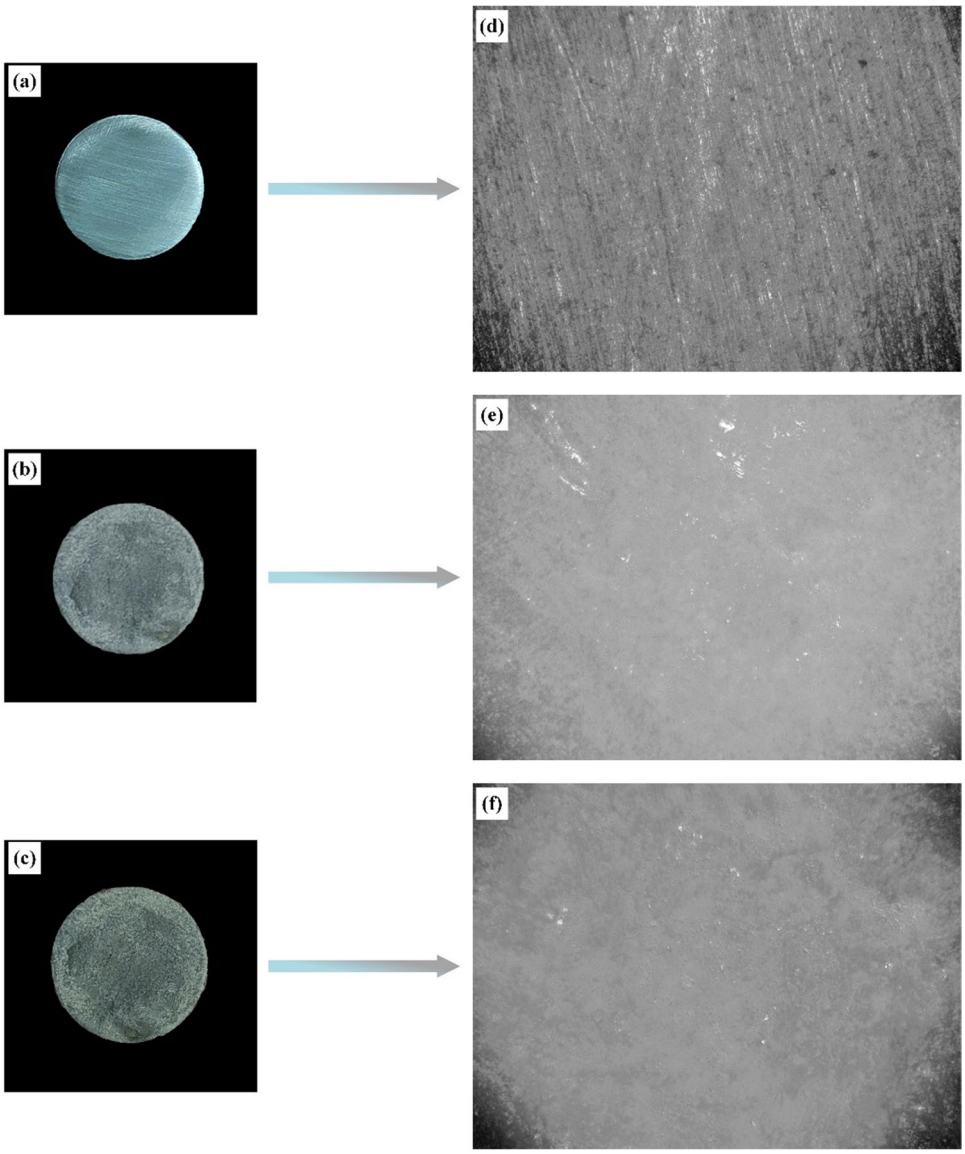

Fig. 5 Zinc anode sheet surface image. **a–c** The surface of zinc anode sheet without reaction, after reaction in 2M $ZnSO_4$+0.5M $MnSO_4$ electrolyte and after reaction in 2M $ZnSO_4$+0.5M $MnSO_4$+0.3M H_2SO_4 electrolyte, respectively; **d–f a–c** corresponding optical microscope images

of anode zinc flake before reaction, after reaction without adding sulfuric acid, and after reaction with adding sulfuric acid, respectively. Correspondingly, Fig. 5d–f are the images they observed by optical microscope. There was no significant difference in the surface characteristics of the reacted zinc flakes with or without the addition of sulfuric acid. Compared to the pre-reaction period, the Zn surface showed white products and surface scratches were reduced (the scratches on the zinc flakes were caused by sandpaper polishing). This indicates that the zinc anode is relatively stable in the electrolyte used in this experiment, which is the basis for the excellent electrochemical performance of the batteries in this study.

Conclusion

In summary, in this paper, the prepared β-MnO_2/3D GPE-CNT cathode materials were used, and H_2SO_4 was added to the electrolyte to regulate the electrolyte pH. Combined with XRD, SEM, TEM, XPS, specific surface area tests, and various electrochemical testing methods, we found that the excellent characteristics of the cathode materials, such as low crystallinity, minimal agglomeration, small particle size, and large specific surface area, have enabled the successful deepening of the two-electron conversion pathway of MnO_2/Mn^{2+} by adding H_2SO_4 to the electrolyte. This enhancement has effectively increased the specific capacity of the batteries, resulting in batteries with good cycling stability. The results indicate that the batteries exhibit a high diffusion rate of Zn^{2+}, an increased working potential, and a more profound level of two-electron conversion under acidic conditions conducive to a specific pH range. With 2.0 M $ZnSO_4$ + 0.5 M $MnSO_4$ + 0.1 M H_2SO_4 as the electrolyte, the batteries exhibited a reversible discharge-specific capacity of up to 536.07 $mAh{\cdot}g^{-1}$ at 100 $mA{\cdot}g^{-1}$. The activated batteries showed a reversible specific capacity of up to 85.11 $mAh{\cdot}g^{-1}$ even at a high current density of 1 $A{\cdot}g^{-1}$, with a capacity retention rate of 88.3% after 1000 cycles. This study offers an effective solution for the practical implementation of AZIBs in the power grid.

Funding We received financial support from the following: Natural Science Foundation of Hebei Province, China (E2021201032); 2024 Hebei University Student Innovation and Entrepreneurship Training project (DC2024258, DC2024259); Ministry of Education's "Spring Fai Project" cooperative research project (202200397); Hebei University 2022 Laboratory Opening Project (sy202266).

Declarations

Competing interests The authors declare no competing interests.

References

1. Cheng AL, Fuchs ERH, Karplus VJ et al (2024) Electric vehicle battery chemistry affects supply chain disruption vulnerabilities. Nat Commun 15(1):2143. https://doi.org/10.1038/s41467-024-46418-1
2. Larcher D, Tarascon JM (2015) Towards greener and more sustainable batteries for electrical energy storage. Nat Chem 7(1):19–29. https://doi.org/10.1038/nchem.2085
3. Harper G, Sommerville R, Kendrick E et al (2019) Recycling lithium-ion batteries from electric vehicles. Nature 575(7781):75–86. https://doi.org/10.1038/s41586-019-1682-5
4. Liu B, Jia Y, Yuan C et al (2020) Safety issues and mechanisms of lithium-ion battery cell upon mechanical abusive loading: a review. Energy Storage Mater 24:85–112. https://doi.org/10.1016/j.ensm.2019.06.036
5. Zhang X, Li J, Ao H et al (2020) Appropriately hydrophilic/hydrophobic cathode enables high-performance aqueous zinc-ion batteries. Energy Storage Mater 30:337–345. https://doi.org/10.1016/j.ensm.2020.05.021
6. Sun Z, Bu F, Zhang Y et al (2024) Electron-donating conjugation effect modulated Zn^{2+} reduction reaction for separator-free aqueous zinc batteries. Angew Chem Int Ed Eng:e202402987. https://doi.org/10.1002/anie.202402987
7. Chamoun M, Brant WR, Tai C-W et al (2018) Rechargeability of aqueous sulfate Zn/MnO_2 batteries enhanced by accessible Mn^{2+} ions. Energy Storage Mater 15:351–360. https://doi.org/10.1016/j.ensm.2018.06.019
8. Cao Z, Zhu X, Xu D et al (2021) Eliminating Zn dendrites by commercial cyanoacrylate adhesive for zinc ion battery. Energy Storage Mater 36:132–138. https://doi.org/10.1016/j.ensm.2020.12.022
9. Cao J, Wu H, Zhang D et al (2024) In-situ ultrafast construction of zinc tungstate interface layer for highly reversible zinc anodes. Angew Chem Int Ed. https://doi.org/10.1002/anie.202319661
10. Ming J, Guo J, Xia C et al (2019) Zinc-ion batteries: materials, mechanisms, and applications. Mater Sci Eng R Rep 135:58–84. https://doi.org/10.1016/j.mser.2018.10.002
11. Wang D, Wang L, Liang G et al (2019) A superior delta-MnO_2 cathode and a self-healing Zn-delta-MnO_2 battery. ACS Nano 13(9):10643–10652. https://doi.org/10.1021/acsnano.9b04916
12. Liu Y, Wu X (2022) Strategies for constructing manganese-based oxide electrode materials for aqueous rechargeable zinc-ion batteries. Chin Chem Lett 33(3):1236–1244. https://doi.org/10.1016/j.cclet.2021.08.081
13. Xia C, Guo J, Li P et al (2018) Highly stable aqueous zinc-ion storage using a layered calcium vanadium oxide bronze cathode. Angew Chem Int Ed Eng 57(15):3943–3948. https://doi.org/10.1002/anie.201713291
14. Wan F, Zhang L, Dai X et al (2018) Aqueous rechargeable zinc/sodium vanadate batteries with enhanced performance from simultaneous insertion of dual carriers. Nat Commun 9(1):1656. https://doi.org/10.1038/s41467-018-04060-8
15. Chao D, Zhu CR, Song M et al (2018) A high-rate and stable quasi-solid-state zinc-ion battery with novel 2D layered zinc orthovanadate array. Adv Mater 30(32):e1803181. https://doi.org/10.1002/adma.201803181
16. Li K, Liu Y, Wu X (2023) Mn^{2+} Intercalation into hydrated vanadium pentoxide nanosheets for highly durable zinc ion batteries. ACS Appl Nano Mater 6(13):12439–12446. https://doi.org/10.1021/acsanm.3c02148
17. Cao J, Zhang D, Chanajaree R et al (2024) A low-cost separator enables a highly stable zinc anode by accelerating the de-solvation effect. Chem Eng J 480. https://doi.org/10.1016/j.cej.2023.147980

18. Zhang L, Chen L, Zhou X et al (2014) Towards high-voltage aqueous metal-ion batteries beyond 1.5 V: the zinc/zinc hexacyanoferrate system. Adv Energy Mater 5(2). https://doi.org/10.1002/aenm.201400930
19. Yu F, Pang L, Wang X et al (2019) Aqueous alkaline–acid hybrid electrolyte for zinc-bromine battery with 3V voltage window. Energy Storage Mater 19:56–61. https://doi.org/10.1016/j.ensm.2019.02.024
20. Lv W, Shen Z, Li X et al (2024) Discovering cathodic biocompatibility for aqueous Zn-MnO_2 battery: an integrating biomass carbon strategy. Nano Lett 16(1):109. https://doi.org/10.1007/s40820-024-01334-3
21. Li C, Kingsbury R, Thind AS et al (2023) Enabling selective zinc-ion intercalation by a eutectic electrolyte for practical anodeless zinc batteries. Nat Commun 14(1):3067. https://doi.org/10.1038/s41467-023-38460-2
22. Shi M, Zhu H, Chen C et al (2022) Synergistically coupling of graphene quantum dots with Zn-intercalated MnO_2 cathode for high-performance aqueous Zn-ion batteries. Int J Miner Metall Mater 30(1):25–32. https://doi.org/10.1007/s12613-022-2441-4
23. Cao J, Zhang D, Zhang X et al (2020) Mechanochemical reactions of MnO_2 and graphite nanosheets as a durable zinc ion battery cathode. Appl Surf Sci 534. https://doi.org/10.1016/j.apsusc.2020.147630
24. Liu C, Xie X, Lu B et al (2021) Electrolyte strategies toward better zinc-ion batteries. ACS Energy Lett 6(3):1015–1033. https://doi.org/10.1021/acsenergylett.0c02684
25. Zhou M, Chen Y, Fang G et al (2022) Electrolyte/electrode interfacial electrochemical behaviors and optimization strategies in aqueous zinc-ion batteries. Energy Storage Mater 45:618–646. https://doi.org/10.1016/j.ensm.2021.12.011
26. Geng Y, Pan L, Peng Z et al (2022) Electrolyte additive engineering for aqueous Zn ion batteries. Energy Storage Mater 51:733–755. https://doi.org/10.1016/j.ensm.2022.07.017
27. Abdulla J, Cao J, Zhang D et al (2021) Elimination of zinc dendrites by graphene oxide electrolyte additive for zinc-ion batteries. ACS Appl Energy Mater 4(5):4602–4609. https://doi.org/10.1021/acsaem.1c00224
28. Zhang Q, Yang Z, Ji H et al (2021) Issues and rational design of aqueous electrolyte for Zn-ion batteries. SusMat 1(3):432–447. https://doi.org/10.1002/sus2.20
29. Chen H, Dai C, Xiao F et al (2022) Reunderstanding the reaction mechanism of aqueous Zn-Mn batteries with sulfate electrolytes: role of the zinc sulfate hydroxide. Adv Mater 34(15):e2109092. https://doi.org/10.1002/adma.202109092
30. Zhang Y, Fu X, Ding Y et al (2024) Electrolyte solvation chemistry for stabilizing the Zn anode via functionalized organic agents. Small:e2311407. https://doi.org/10.1002/smll.202311407
31. Nie W, Cheng H, Sun Q et al (2023) Design strategies toward high-performance Zn metal anode. Small Methods:e2201572. https://doi.org/10.1002/smtd.202201572
32. Cao J, Zhang D, Zhang X et al (2022) Strategies of regulating Zn^{2+} solvation structures for dendrite-free and side reaction-suppressed zinc-ion batteries. Energy Environ Sci 15(2):499–528. https://doi.org/10.1039/d1ee03377h
33. Hu P, Zhu T, Wang X et al (2019) Aqueous Zn//Zn$(CF_3SO_3)_2$//$Na_3V_2(PO_4)_3$ batteries with simultaneous Zn^{2+}/Na^+ intercalation/de-intercalation. Nano Energy 58:492–498. https://doi.org/10.1016/j.nanoen.2019.01.068
34. Xu X, Song M, Li M et al (2023) A novel bifunctional zinc gluconate electrolyte for a stable Zn anode. Chem Eng J 454. https://doi.org/10.1016/j.cej.2022.140364
35. Deng Z, Huang J, Liu J et al (2019) β-MnO_2 nanolayer coated on carbon cloth as a high-activity aqueous zinc-ion battery cathode with high-capacity and long-cycle-life. Mater Lett 248:207–210. https://doi.org/10.1016/j.matlet.2019.04.036
36. Zhang T, Tang Y, Fang G et al (2020) Electrochemical activation of manganese-based cathode in aqueous zinc-ion electrolyte. Adv Funct Mater 30(30). https://doi.org/10.1002/adfm.202002711
37. Zhong Y, Cheng Z, Zhang H et al (2022) Monosodium glutamate, an effective electrolyte additive to enhance cycling performance of Zn anode in aqueous battery. Nano Energy 98. https://doi.org/10.1016/j.nanoen.2022.107220
38. Sun P, Ma L, Zhou W et al (2021) Simultaneous regulation on solvation shell and electrode interface for dendrite-free Zn ion batteries achieved by a low-cost glucose additive. Angew Chem Int Ed Eng 60(33):18247–18255. https://doi.org/10.1002/anie.202105756
39. Wang B, Zheng R, Yang W et al (2022) Synergistic solvation and interface regulations of eco-friendly silk peptide additive enabling stable aqueous zinc-ion batteries. Adv Funct Mater 32(23). https://doi.org/10.1002/adfm.202112693
40. Miao Z, Liu Q, Wei W et al (2022) Unveiling unique steric effect of threonine additive for highly reversible Zn anode. Nano Energy 97. https://doi.org/10.1016/j.nanoen.2022.107145
41. Hao J, Yuan L, Zhu Y et al (2022) Triple-function electrolyte regulation toward advanced aqueous Zn-ion batteries. Adv Mater 34(44):e2206963. https://doi.org/10.1002/adma.202206963
42. Cao J, Wu JX, Wu HY et al (2024) Dendrite-free zinc anode via oriented plating with alkaline earth metal ion additives. Adv Funct Mater. https://doi.org/10.1002/adfm.202401537
43. Zhang Y, Li M, Li H et al (2023) Catholyte modulation and Prussian blue/Berlin green redox mediator enabling efficient high-potential Mn^{2+}/MnO_2 reaction for aqueous hybrid batteries. Small Struct 5(1). https://doi.org/10.1002/sstr.202300257
44. Yang M, Chen R, Shen Y et al (2020) A high-energy aqueous manganese-metal hydride hybrid battery. Adv Mater 32(38):e2001106. https://doi.org/10.1002/adma.202001106
45. Li G, Huang Z, Chen J et al (2020) Rechargeable Zn-ion batteries with high power and energy densities: a two-electron reaction pathway in birnessite MnO_2 cathode materials. J Mater Chem A 8(4):1975–1985. https://doi.org/10.1039/c9ta11985j
46. Zeng X, Liu J, Mao J et al (2020) Toward a reversible Mn^{4+}/Mn^{2+} redox reaction and dendrite-free Zn anode in near-neutral aqueous Zn/MnO_2 batteries via salt anion chemistry. Adv Energy Mater 10(32). https://doi.org/10.1002/aenm.201904163
47. Zhong Z, Li J, Li L et al (2022) Improving performance of zinc-manganese battery via efficient deposition/dissolution chemistry. Energy Storage Mater 46:165–174. https://doi.org/10.1016/j.ensm.2022.01.006
48. Xin S, Dong X, Jin D et al (2023) β-MnO_2/three-dimensional graphene-carbon nanotube hybrids as cathode for aqueous zinc-ion battery. J Alloys Compd 968. https://doi.org/10.1016/j.jallcom.2023.172115
49. Jin D, Dong X, Xin S et al (2024) Effect of $MnSO_4$ concentration on the electrochemical performance of β-MnO_2/3D graphene-carbon nanotube hybrids cathode for aqueous zinc-ion batteries. Ionics. https://doi.org/10.1007/s11581-024-05537-x
50. Chao D, Zhou W, Ye C et al (2019) An electrolytic Zn-MnO_2 battery for high-voltage and scalable energy storage. Angew Chem

Int Ed Eng 58(23):7823–7828. https://doi.org/10.1002/anie.201904174
51. Bischoff CF, Fitz OS, Burns J et al (2020) Revealing the local pH value changes of acidic aqueous zinc ion batteries with a manganese dioxide electrode during cycling. J Electrochem Soc 167(2). https://doi.org/10.1149/1945-7111/ab6c57
52. Pan H, Shao Y, Yan P et al (2016) Reversible aqueous zinc/manganese oxide energy storage from conversion reactions. Nat Energy 1(5). https://doi.org/10.1038/nenergy.2016.39
53. Zang X, Shen C, Sanghadasa M et al (2018) High-voltage supercapacitors based on aqueous electrolytes. ChemElectroChem 6(4):976–988. https://doi.org/10.1002/celc.201801225
54. Kataoka F, Ishida T, Nagita K et al (2020) Cobalt-doped layered MnO_2 thin film electrochemically grown on nitrogen-doped carbon cloth for aqueous zinc-ion batteries. ACS Appl Energy Mater 3(5):4720–4726. https://doi.org/10.1021/acsaem.0c00357